Atomistic modeling of displacement cascades in $La_2Zr_2O_7$ pyrochlore

Alain Chartier* and Constantin Meis†
CEA-Saclay DEN/DPC/SCP Bât. 450Sud, 91191 Gif-Sur-Yvette, France

Jean-Paul Crocombette
CEA-Saclay DEN/DMN/SRMP Bât. 520, 91191 Gif-Sur-Yvette, France

L. René Corrales‡ and William J. Weber
Pacific Northwest National Laboratory, P.O. Box 999, Richland, Washington 99352
(Received 15 October 2002; revised manuscript received 24 January 2003; published 8 May 2003)

An empirical potentials molecular dynamics method was used to simulate the α-recoil effects in the lanthanum zirconate pyrochlore $La_2Zr_2O_7$, at 350 K, where a tetravalent uranium ion was used as the primary knock-on atom with a kinetic energy of 6 keV. The displacement cascades simulations have been carried out along four different crystallographic directions. A detailed analysis indicates that the primary damage state associated with the cascades remains crystalline and consists of point defects, such as cations antisites configurations, various interstitials, and vacancies. There is no evidence for direct amorphization within the cascades. The results are consistent with experimental evidence as well as with previous theoretical work based on static calculations.

DOI: 10.1103/PhysRevB.67.174102 PACS number(s): 61.80.−x, 65.40.−b, 62.20.−x

I. INTRODUCTION

Pyrochlores are ceramics having the general formula $A_2B_2O_7$, where A and B are metallic cations that can be either trivalent and tetravalent or divalent and pentavalent, respectively.[1] Lixiviation studies have shown that the zirconate pyrochlores $A_2Zr_2O_7$, where A is generally a rare-earth element, are extremely durable materials,[2–5] exhibiting leaching rates as low as 10^{-5} g m^{-2} day^{-1} at pH$\sim$7. Recent experimental studies[6] have demonstrated that the titanate-zirconate pyrochlore $Gd_2Ti_{2-x}Zr_xO_7$ becomes more radiation resistant with increasing zirconium concentration. Hence, the purely titanate end member pyrochlore ($x=0$) is sensitive to irradiation damage and readily undergoes an irradiation-induced crystalline to amorphous transition at temperatures up to relatively high temperature (900 K) at doses as low as 0.2 dpa. In contrast, the pure zirconate end member ($x=2$) is rather insensitive to irradiation damage and remains highly crystalline to high doses (up to 7.0 dpa) even at very low temperature ($\sim$25 K), undergoing a radiation-induced transition to the disordered fluorite structure, which is highly radiation resistant. An equivalent behavior has been observed experimentally for the $Er_2Zr_2O_7$ pyrochlore.[7] Because actinide cations may be easily substituted for the rare-earth elements,[8] the zirconate pyrochlores have been proposed[9] as actinide-bearing host phases within the framework of nuclear waste disposal and as inert matrix for industrial and military grade plutonium incineration.[10]

In order to explain the radiation resistance of the zirconate pyrochlores, it has been argued[6,7] that the final radiation state of such a compound is mainly composed of a high number of cation antisite configurations with a random occupancy of the oxygen crystallographic sites 48f, 8b, and 8a (Fig. 1). Such a structure is considered to be close to that of cubic zirconia ZrO_2, stabilized by a rare-earth oxide A_2O_3 (A = Gd, Er, ...), similar to the Y_2O_3 stabilized zirconia (YSZ), which is extremely radiation resistant.[11] That trend seems to be further enhanced by the structure of the end members solid solution of the zirconate pyrochlores A_2O_3 and ZrO_2.[12] Thus for example, Gd_2O_3 has the bixbyite structure, which is cubic and closely related to the fluorite one, involving no significant lattice destabilization of the matrix. Conversely, TiO_2 has the rutile structure, which is essentially different to the fluorite as well as to the bixbyite structure, imparting a strong destabilization of the matrix symmetry.

Many theoretical studies, based exclusively upon energy calculations of static configurations, have been done[7,13–19] in order to draw out the relevant trends that could explain the radiation behavior of the pyrochlores with respect to their chemical composition. It has been advanced that the propensity of a pyrochlore to undergo a transition to the amorphous state is closely related to the cation antisite defect formation energies,[7] which are strongly dependent on the trivalent and tetravalent cation ionic radii.[7,17] Thus, the lower the cation

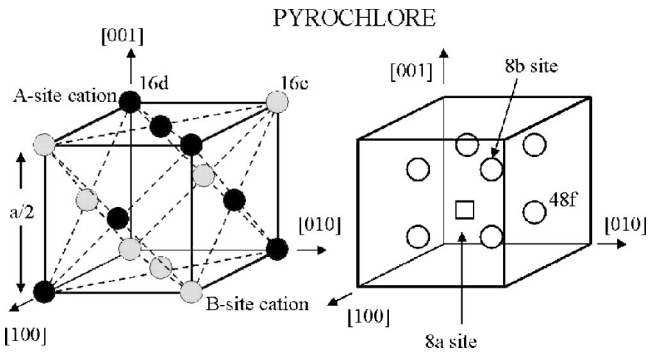

FIG. 1. The $La_2Zr_2O_7$ pyrochlore structure separated into cation and anion sublattices. Zirconium occupies the 16c site while lanthanum the 16d one. The natural oxygen vacancy is in the 8a site, while the oxygen at the 8b site is tetrahedrally coordinated with four lanthanum cations. The center of this cube is the 32e site.

antisite formation energies, the easier the pyrochlore transforms under irradiation to the disordered fluorite structure, hence the more radiation resistant it becomes. Applying *ab initio* calculations, within both the self-consistent field Hartree-Fock computational scheme and the density functional theory (DFT) within the local density approximation (LDA) approach, we have shown[20] the La-Zr cation antisite ($1X$) formation energy in the $La_2Zr_2O_7$ pyrochlore to be rather low, about $E(1X)=2$ eV. Furthermore, this value decreases with increasing cation disorder, which also favors the oxygen occupancy of the $8a$ vacant site (Fig. 1). Consequently, the $La_2Zr_2O_7$ should be expected to be very radiation resistant, since the disordered fluorite state should be easily induced under irradiation at very low energy cost. However, according to recent experiments,[21] the $La_2Zr_2O_7$ seems to be the only zirconate pyrochlore that, under irradiation, undergoes an intermediate transition to the disordered fluorite state prior to becoming amorphous at low temperatures ($T<310$ K); however, under irradiation at higher temperatures, this material retains the crystalline fluorite disordered structure. Thus, based on experimental results, the primary damage state induced in pristine $La_2Zr_2O_7$, over a wide range of temperatures, is a fluoritelike structure with little, if any, amorphous material produced. This particular behavior is consistent with the static calculations on the defect formation energies; however, these results demonstrate that the disordered fluorite structure itself is not sufficient to prevent amorphization in $La_2Zr_2O_7$ under extended irradiation. While the static calculations correctly predict the ease of transformation to the disordered fluorite structure, these calculations do not take into account the activation energies for relaxation of irradiation-induced defects, the effects of high concentrations, nor the effects of temperature and pressure on the creation and annealing of defects. Consequently, an extended investigation of the dynamic processes during atomic displacement cascades, taking into account the temperature of the system, is necessary to understand the principal mechanisms responsible for the transition towards the disordered fluorite and then to the amorphous state.

In this paper, we present the results of molecular dynamics (MD) simulations of atomic displacement cascades (DC's) in $La_2Zr_2O_7$, at 350 K. While the simulation temperature is above the critical temperature for amorphisation determined to be $T_c\sim 310$ K under a given set of experimental conditions,[21] the simulation times are too short to allow the diffusive recovery processes to occur that drive the determination of T_c; thus, the primary damage state produced in these simulations should be representative of the primary damage state for a range of temperatures above and below T_c. Planned simulations over a range of temperatures will determine the significance of temperature on the primary damage state. In the first step of this theoretical study, we establish hard-core ionic interaction potentials, appropriate for the DC simulations, using the GULP code.[22] The resulting force field is further validated by comparing various calculated physical properties of the $La_2Zr_2O_7$ structure, including sound velocity and thermal conductivity, to experimental values in the literature. We then calculate the formation energies for Frenkel pairs and cation antisite defects in both the ordered and disordered structure, as well as the threshold displacement energies along different crystallographic directions. Finally, we perform MD simulations of the α recoil along four nonequivalent crystallographic directions using a $^{238}U^{4+}$ ion at 6 keV and applying the NDM-90 code.[23] The analysis of these results will provide important insights into the primary damage state produced in $La_2Zr_2O_7$ over a range of temperatures where defect diffusion processes are long compared to the simulation times.

II. ANALYTIC INTERATOMIC POTENTIALS (AIP'S)

A. Establishing rigid-core AIP for $La_2Zr_2O_7$

The cubic zirconate pyrochlore structure has the space group $Fd\bar{3}m$ and derives from the MO_2 ($M=$Zr, Ce, U, . . .) fluoritelike arrangement of atoms.[24,25] In $La_2Zr_2O_7$, as illustrated in Fig. 1, the La^{3+} cations occupy the special crystallographic site $16d$ (1/2,1/2,1/2)(A site) and the Zr^{4+} ones the special site $16c$ (0,0,0)(B site). The two independent O^{2-} are located at the $48f$ (x,1/8,1/8), denoted O_{48f}, and $8b$ (3/8,3/8,3/8), denoted O_{8b} sites. Thus, the cubic pyrochlore structure can be described by two independent parameters: the internal parameter x for the $48f$ oxygen positions and the cell parameter a. The unfilled $8a$ site (1/8,1/8,1/8) is the site of the missing oxygen in the pyrochlore structure and is denoted O_{8a}. The occupation of the $8a$ vacant site by oxygen, which leads to a fluorite-type anion sublattice, increases with the temperature and also with increasing cation antisite disorder.[20] The $32e$ site at (1/4, 1/4,1/4) is a natural interstitial site for cations.

With the aim of performing reliable MD-DC simulations, the modeling of the interatomic interactions in $La_2Zr_2O_7$ pyrochlore demands a reliable force field capable of reproducing not only the crystallographic properties but also the elastic and thermodynamic properties, the heat conductivity, and defect formation energies. It is of utmost importance that the ionic interactions during the ballistic process be described with convenient precision not only around the equilibrium positions, but also at intermediate distances and for interstitial sites. In fact, during the α-recoil process, a large number of atomic displacements occur that entail the creation of various defects while the matrix experiences a significant local variation of temperature and pressure. Consequently, a poor representation of the energetic pathways in the structure, and of the defect formation energies, could lead to an inaccurate configuration of the damage structure created by the kinetic energy dissipated by the recoiling ion. Furthermore, a very high (or low) value of the bulk modulus could unphysically alter the structure resistance to damage,[26–28] while poor thermal conductivity could strongly affect the number and the nature of the defects created during the thermal spike, as argued in metals and dielectrics.[29,30]

We assume the interactions to be purely ionic using Buckingham potentials for the description of the short-range interactions to complement the Coulomb interactions. As is well known, Buckingham potentials are composed by a Born-Mayer repulsive exponential term and an r^{-6} attractive one. Cation-cation interactions, other than the electrostatic

TABLE I. Parameters for the Buckingham potentials fitted on experimental crystallographic data and Hartree-Fock calculated elastic constants (Ref. 20). The O-O parameters have been fixed to those optimized by Catlow (Ref. 31) and the U-O parameters come from Karakasidis and Lindan (Ref. 53).

Interactions	A(eV)	ρ (Å)	C(eV Å^6)	Charges
O - O (Ref. 31)	22764.30	0.14900	27.89	O: −2
La - O	1367.41	0.35910	0.00	La: +3
Zr - O	1478.69	0.35542	0.00	Zr: +4
U - O (Ref. 53)	895.60	0.42512	65.40	U: +4

ones, are set to zero. The ionic polarizability is neglected here to avoid computational problems and reduce computational costs during the displacement cascade. Charges are set equal to their formal values −2.00, +3.00, and +4.00 for oxygen, lanthanum, and zirconium respectively, which lift the distinction between the 48f and 8b oxygens.[20] The potential parameters optimization is obtained by using a least square procedure minimizing the sum of the squares of the differences between the calculated and the experimental values of the crystal properties as implemented in the GULP code.[22] The O-O Buckingham parameters have been fixed to the values published by Catlow.[31] For the fitting procedure, we have used the experimentally available crystallographic data[32–36] and, in the lack of experimental values, the elastic properties calculated previously within the *ab initio* Hartree-Fock (HF) approach.[20]

The established rigid-core force field is given in Table I, and the calculated properties are in excellent agreement with the experimental and *ab initio* values, as shown in Table II. Furthermore, it is worth noting that the calculated value for the bulk modulus of $La_2Zr_2O_7$, $B=191$ GPa, is physically reasonable when compared to the experimental value $B=205$ GPa for the isostructural $Gd_2Zr_2O_7$ pyrochlore.[37] The calculated IR frequencies, given in Table III, are in good correlation with experiment.[1] The vibration entropy $S_{300\,K}$ was calculated using the phonon spectra, where ten symmetry-unique **k** points across the Brillouin zone were

TABLE II. Comparison between experimental (Refs. 32–36) and calculated data for the $La_2Zr_2O_7$ pyrochlore. HF sets for *ab initio* Hartree-Fock calculations (see Ref. 20), AIP sets for analytic interatomic potentials calculations done with the GULP code (Ref. 22).

$La_2Zr_2O_7$	Exp. (Refs. 32–36)	HF (Ref. 20)	AIP core
V (Å^3)	315.4	331.5	315.4
a (Å)	10.805	10.986	10.805
x	0.4200	0.4198	0.4210
ρ (g cm^{-3})	6.024	5.732	6.024
B (GPa)		191.7	191.4
C_{11} (GPa)		335	338
C_{12} (GPa)		120	118
$S_{300\,K}$ (J/mol K)	240		208
α (10^{-6} K^{-1})	7.0–9.1		6.24
v_L (m/s)			7487

TABLE III. Comparison between experimental (Ref. 1) and core model AIP calculated vibration frequencies for the $La_2Zr_2O_7$ pyrochlore. Assignations have been made by their values.

IR (cm^{-1})	ν_1	ν_2	ν_3	ν_4	ν_5	ν_6
Experiment (Ref. 1)	518	412	352	244/208	176	140
AIP core	540	424	340	271	160	120

considered in carrying out the frequency summation for the partition function. The vibrational entropy $S_{300\,K}$ is in satisfactory agreement with the experimental value[34] just as is the thermal expansion coefficient α,[25,26] calculated by MD simulations (Table II). The entropy derivative versus temperature, at constant pressure, gives immediately the specific heat C_P, which is shown in Fig. 2. The derived C_P values are quite satisfactory although the discrepancies at high temperatures, of the order of 6% compared to the experimental measurements,[34] are mainly due to anharmonic effects. Most of the those physical parameters are slightly more precisely described by the shell model we used in our previous study.[20] The most sensitive effect of the core model simplification is a slightly shifted description of C_p and α.

B. Sound velocity and thermal diffusivity

In the case of cubic symmetry lattices, the compressive waves sound velocity v_L can be immediately deduced using the elastic matrix constants[38] following the expression

$$v_L=\left(\frac{C_{11}}{\rho}\right)^{1/2}=\left(\frac{B+4G/3}{\rho}\right)^{1/2}, \tag{1}$$

where B is the bulk modulus, $G=(C_{11}-C_{12})/2$ is the shear modulus and ρ is the density calculated to be 6.024 g cm^{-3} for $La_2Zr_2O_7$. Using the calculated elastic matrix constants (Table II), we get the value $v_L=7487$ m s^{-1} (Table I) which is quite comparable to 7850 m s^{-1} found for the cubic zirconia ZrO_2 (Ref. 39) and also to the value of 6947 m s^{-1} calculated for the $Gd_2Zr_2O_7$ pyrochlore using the experimen-

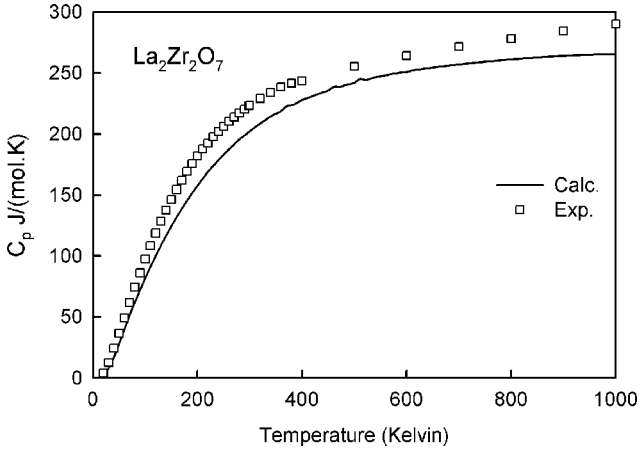

FIG. 2. Heat capacity at constant pressure C_p (J mol^{-1} K^{-1}) versus temperature (K) for the $La_2Zr_2O_7$ pyrochlore. Solid line sets for present AIP core model calculations and open squares are experimental data (Ref. 34).

TABLE IV. Comparison between experimental and calculated heat capacity at constant pressure C_P, density, thermal conductivity κ, and thermal diffusivity D, at 700 K, for $La_2Zr_2O_7$.

$La_2Zr_2O_7$ (700 K)	Experiment	AIP core
C_p (J/mol K)	271.63 (Ref. 34)	256.9
ρ (g cm^{-3})	5.936	5.946
κ (W m^{-1} K^{-1})	2.40 (Ref. 41)	2.88
D (10^{-6} m^2 s^{-1})	0.85 (Ref. 41)	1.05

tal values of $B=205$ GPa and $G=80.3$ GPa (Ref. 37) for the bulk and shear modulus, respectively.

The calculation of the thermal conductivity κ can be carried out by using either the direct or the Green-Kubo method, both based on MD techniques and having generally similar reliability when compared to the experimental values, as recently shown by Schelling and co-workers.[40] Applying the former as described below, we have used a supercell containing 28 160 atoms with the dimensions of 216.13 Å along the x axis and 43.226 Å along the y and z axis. Calculation along one crystallographic direction (x) may be considered as a good approximation since the thermal diffusion in the pyrochlore structure is approximately isotropic.

The direct method based on MD computer simulations are carried out as follows. The simulation box is first equilibrated at 700 K (the temperature for which experimental data are available[41]) by scaling the atomic velocities. The thermal gradient simulations are performed in the NVE microcanonical thermodynamic ensemble by heating the atoms within a slab on the yz plane of 4 Å thickness (along the x axis) where the cell border is centered at the coordinate $x=0$ (and also at $x=216.3\pm2$ Å because periodic boundary conditions are used). Within this slab the thermal energy is increased at the rate of $\Delta\varepsilon/\Delta t=0.1$ K/fs per atom. In order to produce a thermal gradient simultaneously, we cool the atoms in another 4 Å thickness slab also in the yz plane, centered in the middle of the simulation volume, at $x=108.06$ Å, with the thermal energy decreasing at the opposite rate of $\Delta\varepsilon/\Delta t=-0.1$ K/fs per atom. Thus, roughly after 2 ps, a steady thermal flow is established along the x axis between the borders and the middle of the simulation volume. The temperature variation along the x axis is obtained by simply averaging the temperature within thin slabs, 2 Å thick in the yz plane, over the last picosecond of the MD calculations. The obtained $\Delta T/\Delta x$ value equals 2.3 K/Å. The thermal conductivity κ can then be easily determined by setting the heat flow J_x (linear part of the thermal gradient[40]) equal to Fourier's law as follows:

$$J_x=\frac{\Delta\varepsilon}{2A\Delta t}=-\kappa\frac{\partial T}{\partial x}, \tag{2}$$

where $D=\kappa/\rho C_P$ and $A=1868.487$ Å^2 is the simulation volume cross section in the (xy) plane through which propagates the heat flow. We have obtained $\kappa=2.88$ W m^{-1} K^{-1}, in good agreement with the experimental value $\kappa_{\rm exp}=2.40$ W m^{-1} K^{-1}. Using the calculated values of the density ρ and the specific heat C_p at 700 K (Table IV), one gets immediately the thermal diffusivity $D=1.05\times10^{-6}$ m^2 s^{-1} which is comparable to the experimental value of the thermal $D_{\rm exp}=0.85\times10^{-6}$ m^2 s^{-1}(Ref. 41) at 700 K.

C. Formation energy of point defects

As far as we know, no experimental values are available on the formation energies of point defects in the $La_2Zr_2O_7$ pyrochlore structure for further validating the established core-model force field. However, those of cation antisites and Frenkels defects have been calculated in a previous study by *ab initio* methods and more precise shell-model interatomic potentials.[20]

The calculation of defect formation energies is carried out by applying the GULP code,[22] within the Mott-Littleton approximation (MLA).[42] According to this approach, we have considered the crystal volume around the defect to be divided into two concentric spherical regions, with corresponding radius $r_1=9$ Å and $r_2=20$ Å containing, respectively, 206 and 2121 atoms. In the first region, the interactions are treated rigorously and ions are allowed to relax fully. In the second one, only harmonic perturbations are considered. Outside of these two regions is the outer region where the ions interact with the defect net charge as in a perfect dielectric medium. Calculations have also been performed using periodic boundary conditions (PBC's) considering a point defect per primitive lattice (that contains 22 atoms) in order to compare with published results obtained within the DFT/LDA approach.[20] Further comparison can be made between the MLA and the PBC calculations by noting that the former is an isolated defect and the latter is associated with a more dense population of defects. This difference in environment could give insight on the behavior of the ordered pyrochlore because at the beginning of the irradiation the number of defects is sparse and far apart, whereas in the disordered state, observed during irradiation experiments,[21] the defects are found at a higher population and closer together. Knowing the influence of a significant number of closely located cation antisites upon the defects formation energies is quite important. The defect energy is obtained by the classical scheme

$$E(\text{def})=E_{\rm relax}(\text{bulk}+\text{def})-E_{\rm relax}(\text{bulk})+\Delta E_\infty, \tag{3}$$

where ΔE_∞ is a correction energy for the missing species at infinite distance from the crystal. For individual ion defects the last quantity is zero since the potentials are defined with respect to zero energy at infinity. ΔE_∞ also vanishes for cation antisites as well as for Frenkel pair defects, since both the vacancy and the interstitial are present in the bulk.

As previously defined in similar studies,[15–20] $0X$ denotes the perfectly ordered pyrochlore, and $1X$ and $2X$ means single and double La-Zr exchange, respectively. The results for the cation antisite formation energies, calculated within the same computational scheme as in Ref. 20, are presented in Table V. When compared to the DFT/LDA and shell-model AIP calculations, our results show overall satisfactory agreement. Formation energies are nevertheless systemati-

TABLE V. Cation antisite energies (eV) for the compact configuration around the $48f$ site, calculated using a periodic primitive cell containing 22 atoms, with AIP [shell-model (Ref. 20) and core-model] and *ab initio* DFT-LDA (Ref. 20) methods.

$La_2Zr_2O_7$	Mott-Littleton (MLA)		Periodic boundary conditions (PBC's)		
Disorder	AIP core	AIP shell	AIP core	AIP shell	DFT/LDA
$0X$	0.00	0.00	0.00	0.00	0.00
$1X$	2.42	1.95	1.60	1.45	1.38
$2X$	4.67	3.37	4.20	2.79	2.60

cally overestimated by the core model when compared with the shell model, the last being more flexible to accomodate the local distortions of the structure by displacing slightly the shells of the cations or anions. Note that in all cases, the energies $E(1X)$ and $E(2X)$ are lower in the PBC than in the MLA calculations. That follows the trend that a cation antisite inversion in the disordered state, which might correspond to an advanced irradiation stage, may be produced much easier compared to the ordered pyrochlore at the irradiation first stage.

Cation vacancies as well as Frenkel pair formation energies have been calculated and compared with previous results in the ordered pyrochlore and the disordered states (Table VI). As expected, lanthanum vacancies and lanthanum Frenkel pair creation cost considerably less energy compared to those of zirconium. However, the La and Zr Frenkel formation energies are getting close with increasing disorder, i.e., from $0X$ to $2X$.

Note that the formation energy of the pair $O_{8a}^{2-} + V_{48f}^{\cdot\cdot}$ calculated with the core-model potentials, is close to zero (Table VII), in agreement with the previous shell-model calculations,[20] probably because the same charge $-2|e|$ is removed from the pyrochlore structure in both cases.[43] That value is nevertheless in good correlation with the experimental result in the isostructural compound $Gd_2(GaSb)_{0.2}Zr_{1.6}O_7$. [44] The oxygen configuration is mainly driven by the cation configurations characterized by high antisite formation energies compared to the oxygen Frenkel pairs formation energies, which are slightly negative (Table VII). This trend is further supported by the considerable difference between the cation and anion activation energies for lattice migration. Applying the rational function optimization (RFO) method[45] for the saddle point research within the transition state theory, as implemented in the GULP code,[22] the activation energy for the $48f$ oxygen towards the $8a$ vacant site and vice versa in the ordered pyrochlore ($0X$) is calculated to be 0.32 eV, close to the value calculated previously 0.40 eV.[20] Conversely, those characterizing the cation migrations toward homoatomic and hetero-atomic vacancies in the disordered state ($2X$) are calculated to be close to 4 eV, comparable to the values determined experimentally for cation vacancy migration in stabilized zirconia.[46]

Finally, the core-model force field optimized here, with the aim to be used in MD-DC simulations, reproduces satisfactorily the crystallographic and elastic properties of the $La_2Zr_2O_7$ pyrochlore, as well as the main IR frequencies, the constant pressure specific heat, and the thermal expansion coefficient. It is notable that the shell model presented in previous work[20] and the core model used predict very similar properties, even though the former is expected to be somewhat superior. Quite physical values have been also obtained for the compressive waves velocity and the heat conductivity. This could mean that, even though the electron-phonon coupling is completely ignored in such a potential representation, the propagation of the mechanical and thermal perturbation produced by the ballistic process during the thermal spike will be described in a fairly reasonable way. It is also important to note that the values obtained for the various point defects formation and migration energies in the ordered and disordered structure using the core model are in good agreement with those calculated previously with the shell model,[20] a more precise methods. Hence, the established force field can be used with a convenient degree of confidence for the calculation of the threshold displacement energies and for performing MD-DC in $La_2Zr_2O_7$ for the simulation of the α-recoil process.

TABLE VI. Cation vacancies and Frenkel pair formation energies (eV) in different cation antisite disorder configurations, calculated using AIP with core model and compared with previous shell model calculations (Ref. 20). $0X$, $1X$, and $2X$ set for perfect pyrochlore, one La-Zr inversion and two La-Zr inversions, respectively.

Formation energies	$0X$		$1X$		$2X$	
AIP	core	shell	core	shell	core	shell
V_{La}'''	46.61	46.30	46.97	46.37	51.81	48.49
Frenkel La	5.38	7.28	7.25	7.93	8.76	8.99
V_{Zr}''''	87.66	85.88	81.92	85.29	82.69	82.40
Frenkel Zr	14.15	14.93	11.49	12.67	7.24	10.63

TABLE VII. Defect formation energies (eV) for the oxygens in different configurations. The obtained values are also compared to previous shell model calculations (Ref. 20). Symbols are the same as for Table VI.

Formation energies	$0X$		$1X$		$2X$	
AIP	core	shell	core	shell	core	shell
O_{8a}^{2-} interstitial	−14.30	−15.64	−14.19	−15.53	−14.41	−14.96
$V_{O48f}^{\cdot\cdot}$	19.06	18.70	16.71	15.86	16.30	16.80
$V_{O8b}^{\cdot\cdot}$	20.56	19.54	18.32	15.75	20.79	16.75
$V_{O48f}^{\cdot\cdot} + O_{8a}^{2-}$	0.00	−0.05	−0.06	−0.15	−1.50	−1.64

III. THRESHOLD DISPLACEMENT ENERGIES

The threshold displacement energies E_d provide initial insights on the response of atoms to the primary knock-on atom (PKA) ballistic propagation, by characterizing the resistance of a given sublattice to short-range displacements.

TABLE VIII. Calculated threshold displacement energies, in eV, for the atoms of $La_2Zr_2O_7$. The mean values $\langle E_d \rangle$ have been obtained over fourteen different crystallographic directions. $\langle O \rangle_s$ is the stoichiometric mean value for the oxygen. The lower E_d values noted min(E_d) and the corresponding directions $[uvw]$ have been quoted too. Note that min(E_d) for the Zr is in the [111] direction, thus crossing the vacant $8a$ site.

	La	Zr	O_{48f}	O_{8b}	$\langle O \rangle_S$
$\langle E_d \rangle$	153	188	38	68	42
min(E_d)$-[uvw]$	53[$\bar{1}47$]	68 [111]	6.7 [012]	7.0 [114]	

By definition, the E_d corresponds to the minimum kinetic energy transferred by the PKA to an atom along a given crystallographic direction yielding the creation of a stable Frenkel pair defect. The values of E_d provide basic information for modeling radiation effects in materials and may be calculated either by using MD or by applying the sudden approximation (SA) within the MLA. In the MD method,[47] a definite momentum is imparted to an atom along a given crystallographic direction $[uvw]$. After an evolution of a few picoseconds, the system is examined to determine whether the atom is permanently displaced to an interstitial site or not. However, such a process occurs in a time interval much shorter than that needed for relaxation of the lattice through the phonons. Consequently, during the collision of the recoiling atom with the lattice, it can be assumed that the vibrational motion is frozen. This assumption forms the basis of the sudden approximation (SA) method.[48] The SA method does not take into account the dynamic effect of the PKA or the mass ratio effects (heavier/lighter ions) during collisions. However, previous studies on zircon[23,49] as well as on Si and SiC (Ref. 50) have revealed that the E_d values calculated with the SA method to be quite reasonable and comparable to those calculated using the MD methods. Thus, since the SA method is by far less computationally expensive than MD, the former method has been applied here using the GULP code.[22] In the SA method, only static energy calculations are performed. The ion is displaced in a given crystallographic direction $[uvw]$, calculating at each position the total energy of the unrelaxed system. The value of E_d is simply the difference between the minimum energy of the unrelaxed system and that of the perfect bulk provided the displaced ion occupies a stable interstitial position after relaxation. For avoiding complications during relaxation, such as the eventual creation of metastable sites that may be occupied by the displaced atom, the RFO minimization procedure within the MLA framework[42] has been applied here.

As is well known, the value of E_d strongly depends on the crystallographic direction along which the atom is displaced.[51] The [111] direction is for example the path through the ZrO_6 octahedron where E_d for Zr is lower (see Table VIII) since the oxygen $8a$ site is vacant in the perfect pyrochlore. Conversely, this direction is not energetically favorable for the La since the $8b$ site is occupied by an oxygen atom, leading to a direct collision. The lower E_d values for La are obtained along the [$\bar{1}47$] direction (Table VIII), through the LaO_8 scalenohedron. Hence, for extracting the

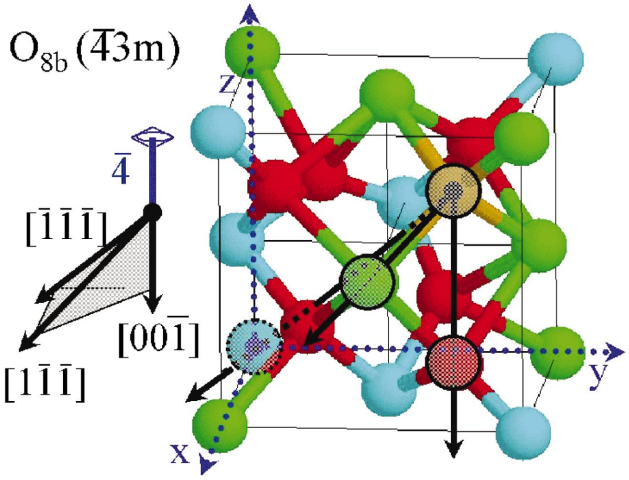

FIG. 3. (Color) The $La_2Zr_2O_7$ pyrochlore structure, where the crystallographic directions delimiting the solid angle for the calculation of the threshold displacement energies for the O_{8b} sublattice, following its symmetry, is quoted. Zirconium and lanthanum are in cyan and green respectively, while O_{48f} are in red and O_{8b} is in light brown.

relevant mean values, it is of crucial importance to consider the highest possible number of representative directions for each of the atomic species La, Zr, O_{48f}, and O_{8b}. Of course, crystallographic directions along which direct ionic collisions occur are not considered in the SA method. In the ordered pyrochlore, such a sampling may be easily simplified by using the site symmetry of the atom considered. Thus, for the O_{8b} having the $\bar{4}3m$ site symmetry, the sampling may be done only in the irreducible part of the total 4π steradians solid angle represented in Fig. 3, for estimating a relevant $\langle E_d(O_{8b}) \rangle >$ value. Fourteen directions have been considered in this case, ranging from [$\bar{1}\bar{1}1$], where no direct collision is expected, to directions close to [$1\bar{1}\bar{1}$] and close to [$00\bar{1}$], where direct collisions with the La should occur during a ballistic process. In the same way, the solid angle that has been considered for the La and Zr, lying, respectively, in $16d$ and $16c$ crystallographic site, is reduced with respect to their $.\bar{3}m$ site symmetry to directions between [111], [$\bar{2}11$], and [$11\bar{2}$]. For the O_{48f}, the solid angle is reduced to the directions included between the planes $x=y$ and $x=-y$, in agreement to its $2.mm$ site symmetry. The calculated mean values that consider fourteen crystallographic directions for each sublattice, together with the lower energy crystallographic directions are given in Table VIII. A considerable amount of energy is needed for displacing the cations while conversely, the oxygen ions may move through specific paths at an extremely low energy cost.

IV. MODELING OF THE α RECOIL IN $La_2Zr_2O_7$

A. Molecular dynamics displacement cascades

The MD-DC simulations of α recoils in $La_2Zr_2O_7$ have been performed using the NDM-90 code.[23] In our case, the established short-range Buckingham potentials, valid within

the interatomic distance range of $1\ \text{Å} < r < 10\ \text{Å}$, are coupled to Ziegler-Biersack-Littmark (ZBL) potentials, valid for $r < 0.9$ Å,[52] by a fifth degree polynomial in the range $0.9\ \text{Å} \leqslant r \leqslant 1.0\ \text{Å}$. The ZBL potentials express more accurately the ionic interactions at very short distances occurring during high-energy collisions. A tetravalent uranium ion is substituted for zirconium in the $La_2Zr_2O_7$ in order to simulate the recoiling nucleus during the α-decay process. To respect the transferability conditions, the U-O Buckingham parameters are fixed to those published by Karakasidis and Lindan[53] that were optimized in UO_2 by using the Catlow interaction potential for O-O.[31] The latter is also used here for the $La_2Zr_2O_7$ modeling.

The atomic trajectories throughout the ballistic process are determined by integrating Newton's equations of motion, using the Verlet algorithm,[54] where the forces derive from the AIP formalism. The integration time step δt is adjustable taking values as low as 5×10^{-17} s, at the beginning of the DC, up to 10^{-15} s at the end. In a first step, a cubic supercell with the characteristic dimension $L = 8a = 129.66$ Å, containing 152064 atoms among which one uranium U^{4+} is substituted for Zr^{4+} at the approximate fractional coordinate (1/4,1/4,1/4) of the supercell, is equilibrated within the NPT ensemble at 350 K by scaling the atomic velocities. After the equilibration stage, the MD calculations are performed at constant volume V with fixed number of particles N. We use periodic boundary conditions and within a border thickness of 4 Å the atomic velocities are continuously scaled during the DC process for simulating a thermal bath at 350 K. The DC calculations are carried out within a microcanonical ensemble that could be denoted as pseudo-(NVE) because the applied thermal bath at the borders contributes in pumping a fractional part of the kinetic energy out of the system.

The mechanical shock-wave produced by the DC propagates through the material with the compressive sound wave velocity. Similar compressive sound wave features have been observed during irradiation experiments in Al_2O_3 and other solids.[28] In the simulations, the periodic boundary conditions act as reflecting walls that can rapidly reflect the mechanical perturbation to the DC area. As shown recently in copper by Ryazanov *et al.*,[55] the local stress tensor fluctuation could have a direct influence upon the atomic displacements and the defects formation. Different numerical methods exist to handle pressure relaxation and pressure transmission on the borders (see Ref. 56, and references therein). Sufficiently large simulation box dimensions have been chosen here for avoiding pressure influence, due to the reflected shock wave, on the thermal spike area. In fact, taking into account the compressive sound waves velocity, calculated above to be $\sim 7500\ \text{m s}^{-1}$, as well as the characteristic dimension of the simulation volume $L = 8a$, the DC induced shock-wave needs about 1.7 ps to come back to the damaged area. This time interval is longer than 1 ps during which, as we shall see, the most important part of the atomic displacements, crystal recovery and defects creation takes place for the typical kinetic energy of 6 keV.

In addition, the heat flux induced by the DC leads to a significant rise of the local temperature within the crystal volume containing the region strongly affected by the ballistic process. Since the calculated values for heat conductivity and the heat diffusivity (Table IV) are very close to the experimental values, the heat flux will propagate quite physically in the bulk, reaching the borders after about 2 ps, where the heat will be smoothly pumped by the thermal bath set up to simulate an infinite crystal at 350 K. To produce an approximate statistical analysis of the $La_2Zr_2O_7$ during a 6 keV ballistic process, four different displacement cascades have been performed along the crystallographic directions [111], [211], [221], and [322].

B. Analysis of the DC in the $La_2Zr_2O_7$ pyrochlore

Snapshots of the cascade simulation projected on the (110) plane for ten time intervals where the U^{4+} is launched in the [111] direction at 6 keV are presented in Fig. 4. The upper border of the periodic cell can be seen on the top of the figure, the three others being truncated to focus on the interesting part of the DC. In the first frame, at $t = 0$ ps, is shown the perfect pyrochlore bulk. During the DC, the highest number of displaced atoms $N_{\text{disp}} = 1069$ is observed approximately at $t_1 = 0.3$ ps. At that time, 807 oxygen, 171 lanthanum, and 91 zirconium ions are displaced by more than 1 Å from their equilibrium positions (Fig. 5 and Table IX). Note that those numbers are directly related to the above calculated E_d and quoted Table VIII, where $E_d(\text{O}) < E_d(\text{La}) < E_d(\text{Zr})$. A fast recovering stage is then observed between $t_1 = 0.3$ and $t_2 = 0.9$ ps during which about 40% of the displaced atoms return to their initial position or occupy equivalent crystallographic sites. A considerably slower evolution stage, mainly involving oxygen thermal annealing, occurs between $t_2 = 0.9$ ps and $t_3 = 3.0$ ps, where roughly 10% of the oxygen atoms displaced to interstitial sites return to crystallographic positions. In fact during the period between $t_2 = 0.9$ ps and $t_3 = 3.0$ ps there is a continuous creation and annealing of oxygen interstitials at the $8a$ site, the annealing rate being more important.

This behavior may be explained by the very high temperature subsisting just after the thermal spike[30] in the closely situated crystal bulk, and by the relatively low activation energy characterizing the transitions $O_{48f}^{2-} \rightarrow V_{8a}$ and $O_{8a}^{2-} \rightarrow V_{48f}^{\cdot\cdot}$, calculated above to be close to $E_m = 0.3$ eV. The transitions $O_{48f}^{2-} \rightarrow V_{48f}^{\cdot\cdot}$ is not considered since its E_m is calculated to be 1.0 eV, which is three times higher. In order to estimate the extend of this effect, we assume that the jump frequency could characterize the corresponding $8a$ vacancy occupation by the $48f$ closely situated oxygen so as we may consider the following expression:[57]

$$\nu(O_{48f} \leftrightarrow V_{8a}) \sim \frac{\prod_i \nu_i}{\prod_m \upsilon_m} \exp(-E_m / k_B T_{\text{ins}}), \qquad (4)$$

where we have taken into account that $\Delta H(V_{8a}) = 0$ and $\Delta H(V_{48f}^{\cdot\cdot} + O_{8a}^{2-}) = 0$ (Table VII) and k_B is Boltzmann's constant. The parameters ν_i are the equilibrium frequencies and ν_m are those with the migration oxygen at the saddle point. Although during the α-recoil process the system is locally

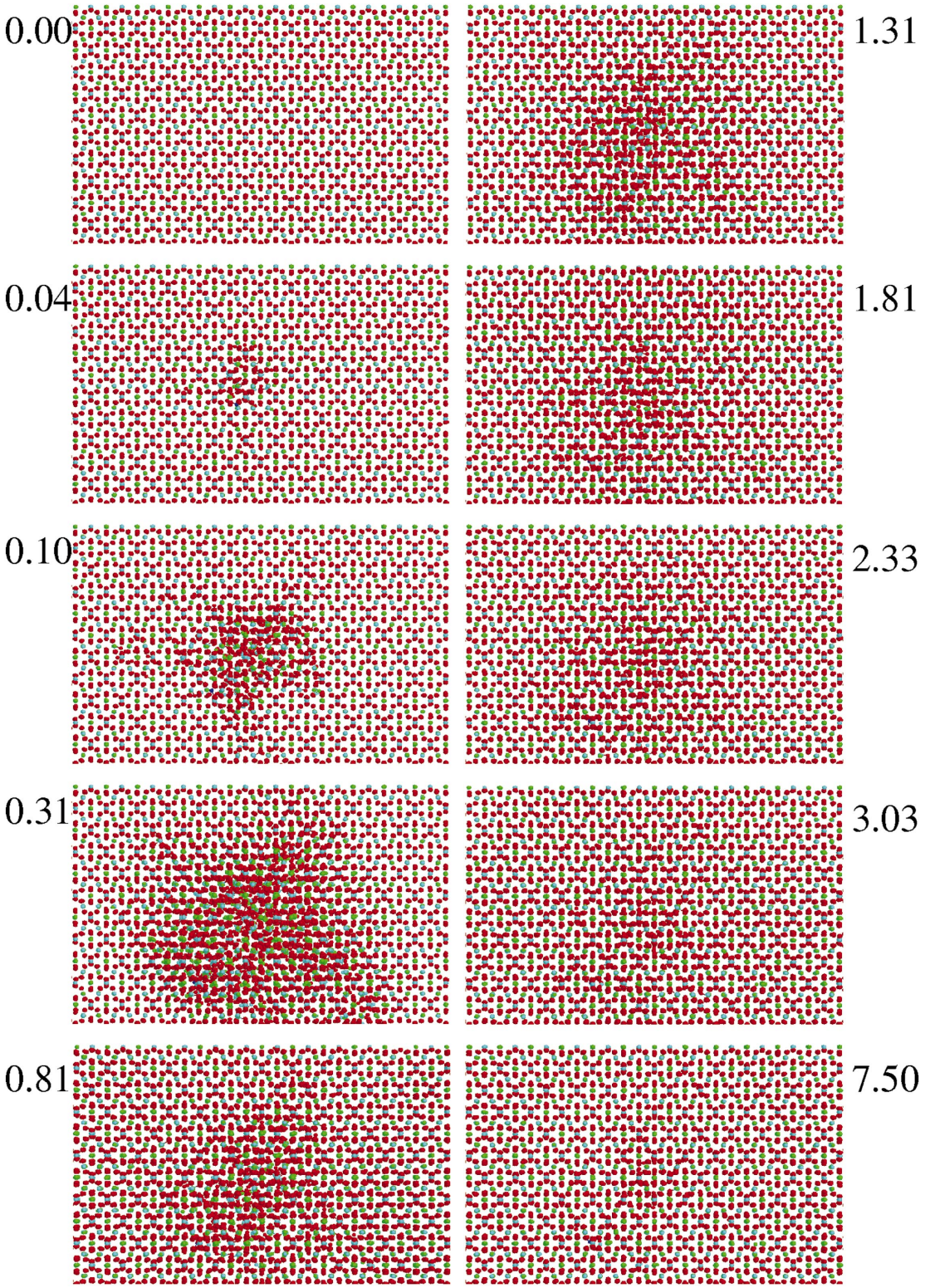

FIG. 4. (Color) View at different times (ps) in the (110) plane of the displacement cascade of a U^{4+} at 6 keV along the direction [111] in the $La_2Zr_2O_7$ pyrochlore, at 350 K. Cyan, green, and red spheres correspond to zirconium, lanthanum, and oxygen atoms, respectively. The uranium atom is in blue.

out of thermodynamic equilibrium, the atomic velocities may be used in order to attribute to the whole supercell an instantaneous temperature T_{ins} according to the relationship $(1/N)\Sigma_{i=1}^{N}\frac{1}{2}m_i v_i^2=\frac{3}{2}k_B T_{\mathrm{ins}}$, where N is the total number of atoms in the simulation volume. Using T_{ins} and the total virial developed according to the energy spatial derivatives, an instantaneous pressure P_{ins} can also be defined.[58] Now, due to a fast collective phenomenon of recovery (see Fig. 5),

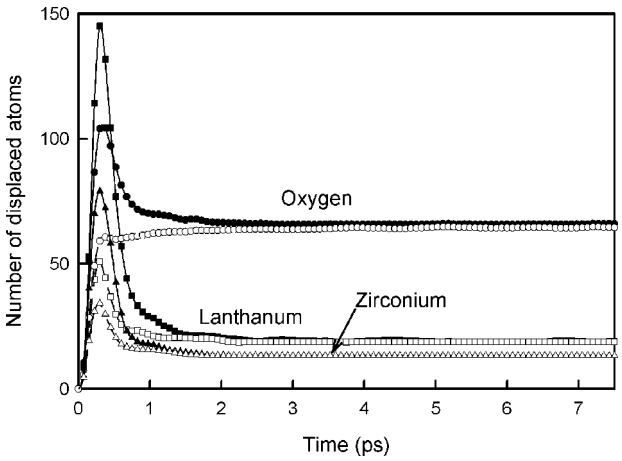

FIG. 5. Number of displaced atoms during the U^{4+} DC at 6 keV along the [111] direction in $La_2Zr_2O_7$, at 350 K. Solid lines (filled symbols) correspond to the atoms displaced by more than 1 Å from their equilibrium positions and dashed lines (open symbols) to those displaced by more than 1.5 Å. Lanthanum, zirconium and oxygen are represented by squares, triangles, and circles, respectively. The number of oxygen ions has been divided by 7.

we may assume the system is establishing a thermodynamic equilibrium roughly after 1 ps. At that time the T_{ins} is about 450 K, over the whole supercell, but a careful analysis of the velocities of about 12 000 atoms around the thermal spike area can easily show the mean local instantaneous temperature to be close to 2000 K such that $\nu(O_{48f} \leftrightarrow V_{8a}, T = 2000\ \mathrm{K}) \sim 10^{12}$ Hz. This jump frequency is high enough for permitting oxygen transitions between the $48f$ and $8a$ sites within a time interval of a few picoseconds. This leads to the conclusion that the oxygen thermal annealing in $La_2Zr_2O_7$ during 3 to 4 ps after the first picosecond of the thermal spike (Fig. 5) is not negligible. In fact, the coordinate analysis within the time interval 1.0 – 4.0 ps shows a dozen oxygen ions occupying the $8a$ vacant site that return to a $48f$ site. Further thermal annealing should be expected to take place at much longer time (hundreds of picoseconds) at lower temperatures. Such a simulation is presently computationally very expensive to be carried out by MD. However, no significant recovering or annealing is observed beyond 4.0 ps up to $t_f = 7.5$ ps. Finally it is worth noting that all the oxygen atoms displaced by less than 1.5 Å return to their equilibrium sites within less than 0.9 ps (Fig. 5).

A similar behavior is realized in all the DC performed along the four crystallographic directions considered here and presented in Table IX. However, a larger number of atoms, about 20 % more, are displaced during the DC along the [111] and [322] directions than along the [211] and [221] directions. This is related with the almost direct impact of the uranium with the lanthanum at the very beginning of the cascade creating different subcascades. This is illustrated in Fig. 6 for the [111] cascade where the uranium suffers its first direct collision with a lanthanum ion. The trajectory of the uranium and lanthanum (first atom scattered by uranium) have been plotted. Conversely, for the two other crystallographic directions, [211], [221] the uranium suffers its first direct collision with an oxygen ion.

The global response of the material is quite similar in any direction, and we may use the mean instantaneous pressures and temperatures of all the four DC's to describe, from a mesoscopic point of view, the general response of the $La_2Zr_2O_7$ pyrochlore to a U^{4+} recoiling ion at 6 keV. In the first 0.25 ps of the DC, the very high velocity of the uranium induces an extremely fast increase of the instantaneous pressure, and the potential energy, and an abrupt decrease of the instantaneous temperature due to the nuclear stopping effect in the material (see Fig. 7). That stage corresponds to a fast increase of the number of displaced atoms, for which the maximum is attained at around 0.3 ps. Due to an inertial collision process, the instantaneous pressure continues rising until 0.45 ps when it attains the value of 1.34 GPa. Meanwhile a part of the stored potential energy is transformed to kinetic energy, thus raising the instantaneous temperature. The T_{ins} increases until 1.4 ps (Fig. 7) reaching the value of 450 K for the whole simulation volume and then, under the effect of the borders thermal bath, it decreases constantly together with the pressure P_{ins}. Of course, all these chronological values depend directly on the size of the simulation box considered and on the pumping rate at the borders. However, the latter parameters have been carefully chosen, as described above, so as not to affect the main part of the DC. Consequently, these characteristic time events should remain roughly identical for bigger simulation volumes and for the same uranium kinetic energy. Hence, this analysis reveals

TABLE IX. Comparison between the maximum number of displaced atoms by more than 1 Å, at t_1 (time in ps at which the maximum disorder is observed) and the number of definitely displaced atoms at the end of the cascades $t_f = 7.5$ ps. All the crystallographic directions of the 6 keV U^{4+} displacement cascades are considered. The d_f means displaced atoms at the end of the DC from which are deduced the atoms in replacement configurations (quoted as equivalent site in Table X). **R**(%) denotes the total recovery and annealing percentage, that is $(t_1 - d_f)/t_1$.

	[111]				[211]				[221]				[322]			
	t_1	t_f	d_f	**R**	t_1	t_f	d_f	**R**	t_1	t_f	d_f	**R**	t_1	t_f	d_f	**R**
	0.32	7.5			0.26	7.5			0.31	7.5			0.29	7.5		
La	171	16	9	**95**	132	21	13	**90**	117	11	8	**93**	178	29	17	**90**
Zr	91	10	8	**91**	67	12	9	**87**	66	9	5	**92**	103	24	15	**85**
O	807	532	64	**92**	711	433	77	**89**	699	408	64	**91**	804	474	58	**93**
Tot.	1069	558	81	**92**	910	466	99	**89**	882	428	77	**91**	1085	527	90	**92**

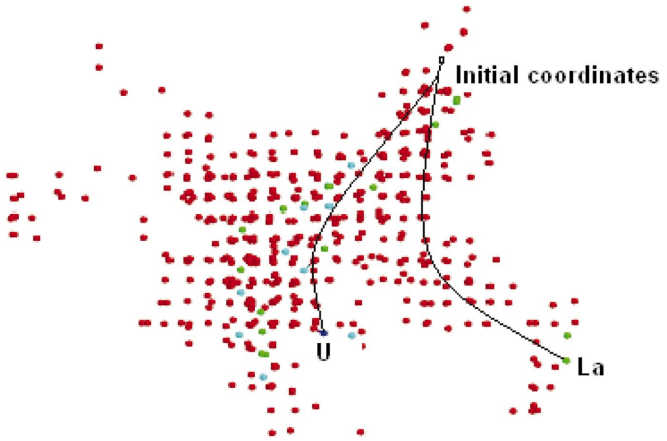

FIG. 6. (Color) Displaced atoms by more than 1 Å at the end of the cascade (7.5 ps) in the (100) plane. The majority of the oxygen atoms (red) occupy equivalent crystallographic sites and then build a squared network. The uranium (blue) trajectory as well as one lanthanum (green) trajectory responsible for a subcascade are shown.

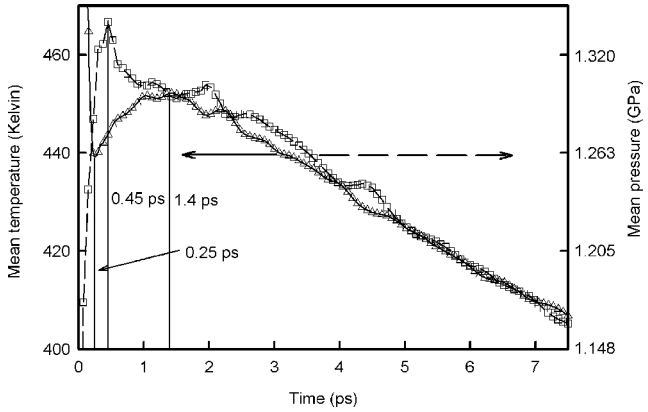

FIG. 7. Evolution of the mean value (over all the DC along the four crystallographic directions) of the instantaneous pressure (squares) and instantaneous temperature (triangles) as a function of time. The local minimum temperature occurs at 0.25 ps while the maximum pressure is attained latter at 0.45 ps. The instantaneous temperature raises to a maximum value at 1.4 ps.

that the DC induces first a strong almost isothermal rise of the pressure followed by oscillations between potential and kinetic energy. The oscillations occur as the energy is pumped out of the cascade region by dissipating the shock wave and the thermal energy at first within the supercell and later by absorption at the boundaries as described above. The net effect is a steady and smooth decrease of pressure and temperature towards the initial conditions.

C. Analysis of the DC end stage

The final number of displaced cations is very low as indicated in Table IX, between 20 (in the [221] direction) and 53 (along the [322] one). Most of the displaced cations form antisite configurations or occupy an equivalent crystallographic site (see Table X). Those cation antisite defects can be seen on the enlargement (see Fig. 8) of the final picture obtained at 7.5 ps (Fig. 4) within the most highly damaged area. Compared to Fig. 4, the projected plane of the Fig. 8 has been slightly tilted in order to display the periodic characteristics of the bulk involving (in this perspective) alternatively oxygen and cation slabs. Two different arrangements can be distinguished in the cation slabs, those containing only La or Zr atoms and those presenting alignments of alternatively La and Zr in the same direction. That makes it easy to distinguish visually the cation antisite defects. Quite a few among the displaced cations, roughly 5 to 10 (Table X) are found at interstitial positions, occupying the 32*e* crystallographic site, and can be easily distinguished in Fig. 8. That trend follows the static calculation results indicating that the cation Frenkel pair formation energies (see Table VI) are considerably higher than the antisites formation energies (see Table V). The same correspondence appears between static and DC calculations of the formation energies of Zr and La Frenkel pairs, and the number of created pairs. By considering only interstitial and cation antisite as relevant defects (thus, a simple replacement configuration is not counted because it does not contribute to the disorder), the cation re-

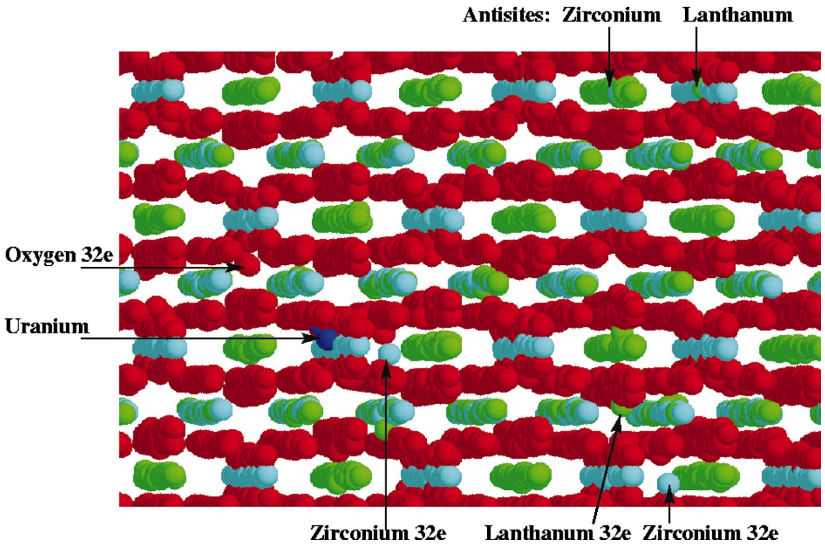

FIG. 8. (Color) Close view of the mostly damaged area after the 6 keV DC in the slightly tilted (110) plane. Alignments or alternation of lanthanum and zirconium can easily be distinguished in the slabs of cations. Point defects such as cation antisites are consequently easily visible, along with interstitials. The U atom ended its course substituted for a zirconium, the last being ejected to a close interstitial site.

TABLE X. Detailed analysis of the nature of the defects created during the U^{4+} DC at 6 keV along the four crystallographic directions considered. More La interstitials are created compared with Zr ones, in agreement with the Frenkel pair formation energies quoted in Table VI.

	[111]	[211]	[221]	[322]
La (Equivalent site)	7	8	3	12
La (Antisite)	6	5	3	9
La (Interstitial, 32*e* site)	3	8	5	8
Zr (Equivalent site)	2	3	4	10
Zr (Antisite)	6	6	2	13
Zr (Interstitial, 32*e* site)	2	3	3	2
O (Equivalent site)	468	356	344	416
O (Interstitial, 8*a* and 32*e* site)	64	77	64	58

covery is close to 90%, independent of the crystallographic direction of the DC (see Table IX).

Compared to cations, a quite large number of oxygen ions are displaced in agreement with the calculated E_d (Table VIII). Most of them, for example 468 out of a total of 532 in the [111] DC, are simply displaced in replacement sequences that have little effect on the crystalline network, as can be seen in Fig. 6. Consequently, these oxygen replacements are not considered as important defects, as discussed above for the cations. Only 64 (in the case of the [111] DC, see Table X) are thus fixed at interstitial sites, mainly the 8*a* site. In some particular configurations after the thermal spike, all the oxygen sites including the 8*a* one are found occupied permitting the formation of an oxygen interstitial in the 32*e* site. Such a situation is presented in Fig. 8. As in the case of the cations, the recovery for the oxygen ions is also found to be around 90%, where the replacement configurations are subtracted from the total displaced atoms (see Table IX). In summary, the analysis of all four DC simulations carried out in this work reveals that an average of about 70 interstitials are produced by a 6 keV uranium pka. The uranium atom ended its course substituted for zirconium, the latter being ejected to a close interstitial site (Fig. 8).

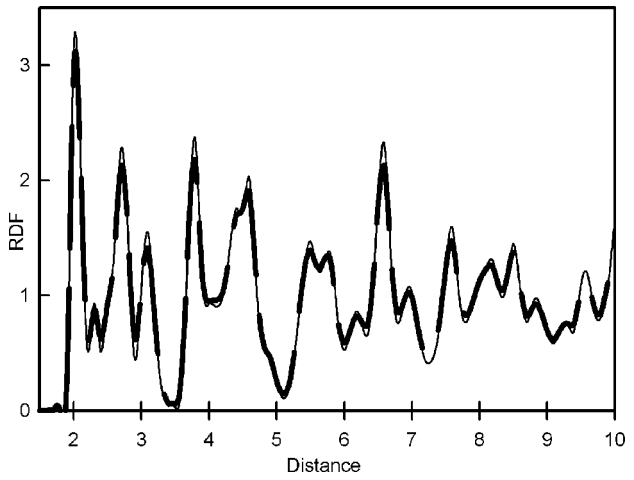

FIG. 9. Radial distribution function comparison before (solid line) and after (dashed line) the DC of U^{4+} at 6 keV launched to the [111] crystallographic direction in the $La_2Zr_2O_7$ pyrochlore.

The final picture obtained at 7.5 ps (Fig. 4) is surprisingly close to the initial state. It correlates the quite small number of defects produced, all localized at crystallographic sites, either interstitials or antisites. The analysis of the radial distribution function (RDF) of the four DC reveals no hint of amorphisation as shown in Fig. 9 for the [111] direction. Both short range and long-range order are preserved. These results are in good agreement with recent experimental works done by Lian *et al.*[21] on $La_2Zr_2O_7$, where an intermediate stage of disordered fluorite structure has been observed over a wide range of temperatures, together with a very high resistance to amorphisation at 350 K.

V. CONCLUSION

We have applied an analytic interatomic potential molecular dynamics method to study the damage profile of displacement cascades produced in $La_2Zr_2O_7$ at 350 K, by a uranium recoiling ion with a kinetic energy of 6 keV. The main conclusion is that at 350 K the lanthanum zirconate pyrochlore preserves its crystalline state during isolated DC events, exhibiting only the formation of cation antisites, interstitials and vacancies at very low yield. For the crystallographic directions considered, th DC simulations show an equivalent behavior, characterized by a very fast recovery phenomenon, during which about 90% of the displaced atoms return to crystallographic sites within less than 1 ps.

The results show that in pristine $La_2Zr_2O_7$ the primary radiation-induced damage state is a transition towards the disordered fluorite state, in good agreement with the experimental results.[21] A significant amount of thermal annealing is observed just after the thermal spike, mainly related to the rapid oxygen mobility towards the 8*a* site characterized by a very low activation energy. Since cation thermal annealing is negligible during the very short simulation time intervals (10–20 ps) employed in these MD-DC simulations, the results suggest that equivalent crystalline states with higher or lower point defect densities may be obtained at lower and higher temperatures, respectively. Hence, from the simulation point of view, the single DC events in $La_2Zr_2O_7$ are unable to induce direct amorphisation in this pyrochlore, at least for low recoiling ion kinetic energies. Complementary calculations using cascade overlap at different temperatures coupled to the study of defects mobility in the resulting damaged areas are required to determine a detailed understanding of the behavior of $La_2Zr_2O_7$ under irradiation.

ACKNOWLEDGMENTS

C.M. and A.C. would like to thank the hospitality L.R.C. and W.J.W. of Pacific Northwest National Laboratory (PNNL) during their visits that allowed this project to be started. L.R.C. would like to thank the hospitality of A.C., C.M., and the CEA-Saclay during his visit that allowed the completion of this work. This work was supported by the Division of Chemical Sciences (LRC), and the Division of

Materials Sciences and Engineering (WJW), Office of Basic Energy Sciences, U.S Department of Energy. Part of this research was performed at the CEA-Saclay, the other was performed in the William R. Wiley Environmental Molecular Sciences Laboratory, a national scientific user facility sponsored by the Department of Energy, Office of Biological and Environmental Research and located at PNNL. Battelle operates PNNL for the U.S. Department of Energy.

*Electronic address: achartier@carnac.cea.fr
†Electronic address: email: cmeis@cea.fr
‡Electronic address: rene.corrales@pnl.gov

[1] M. A. Subramanian, G. Aravamudan, and C. V. Subbs Rao, Prog. Solid State Chem. **15**, 55 (1983).
[2] I. Hayakawa and H. Kamizono, J. Nucl. Mater. **202**, 163 (1993).
[3] G. R. Lumpkin, J. Nucl. Mater. **289**, 136 (2001).
[4] W. J. Weber and R. C. Ewing, Science (Washington, DC, U.S.) **289**, 2051 (2001).
[5] G. R. Lumpkin, K. L. Smith, and M. G. Blackford, J. Nucl. Mater. **289**, 177 (2001).
[6] S. X. Wang, B. D. Begg, L. M. Wang, R. C. Ewing, W. J. Weber, and K. V. Govidan Kutty, J. Mater. Res. **14**, 4470 (1999).
[7] K. E. Sickafus, L. Minervini, R. W. Grimes, J. A. Valdez, M. Ishimaru, F. Li, K. J. McClellan, and T. Hartmann, Science (Washington, DC, U.S.) **289**, 748 (2000).
[8] W. Lutze and R. C. Ewing, *Radioactive Waste Forms for the Future* (North-Holland, Amsterdam, 1988).
[9] R. C. Ewing, W. J. Weber, and W. Lutze, *Disposal of Weapons Plutonium* (Kluwer Academic Publishers, The Netherlands, 1996).
[10] P. E. Raison and R. G. Haire, Prog. Nucl. Energy **38**, 796 (2001).
[11] K. E. Sickafus, H. Matzke, K. Yasuda, P. Chodak, R. A. Verral, P. G. Lucuta, H. R. Andrews, A. Turos, R. Fromknecht, and N. P. Baker, Nucl. Instrum. Methods Phys. Res. B **141**, 358 (1998).
[12] K. E. Sickafus, J. Valdez, J. R. Williams, R. W. Grimes, and H. T. Hawkins, Nucl. Instrum. Methods Phys. Res. B **191**, 549 (2002).
[13] P. J. Wilde and C. R. A. Catlow, Solid State Ionics **112**, 173 (1998).
[14] P. J. Wilde and C. R. A. Catlow, Solid State Ionics **112**, 185 (1998).
[15] R. E. Williford, W. J. Weber, R. Devanathan, and J. D. Gale, J. Electroceram. **3**, 409 (1999).
[16] R. E. Williford, W. J. Weber, R. Devanathan, and J. D. Gale, J. Am. Ceram. Soc. **82**, 3266 (1999).
[17] L. Minervini, R. W. Grimes, and K. E. Sickafus, J. Am. Ceram. Soc. **83**, 1873 (2000).
[18] M. Pirzada, R. W. Grimes, L. Minervini, J. F. Maguire, and K. E. Sickafus, Solid State Ionics **140**, 201 (2001).
[19] R. E. Williford and W. J. Weber, J. Nucl. Mater. **299**, 140 (2001).
[20] A. Chartier, C. Meis, W. J. Weber, and L. R. Corrales, Phys. Rev. B **65**, 134116 (2002).
[21] J. Lian, X. T. Zu, K. V. G. Kutty, J. Chen, L. M. Wang, and R. C. Ewing, Phys. Rev. B **66**, 054108 (2002).
[22] J. D. Gale, J. Chem. Soc., Faraday Trans. **93**, 629 (1997).
[23] J.-P. Crocombette and D. Ghaleb, J. Nucl. Mater. **295**, 167 (2001).
[24] Y. Tabira and R. Withers, Philos. Mag. A **79**, 1335 (1999).
[25] N. K. Kulkarni, S. Sampath, and V. Venugopal, J. Nucl. Mater. **281**, 248 (2000).
[26] H. Trinkaus and A. I. Ryazanov, Phys. Rev. Lett. **74**, 5072 (1995).
[27] C. Trautman, S. Klaumünzer, and H. Trinkaus, Phys. Rev. Lett. **85**, 3648 (2000).
[28] T. Kambara, K. Kageyama, Y. Kanai, T. M. Kojima, Y. Nanai, A. Yoneda, and Y. Yamakazi, Nucl. Instrum. Methods Phys. Res. B **193**, 371 (2002).
[29] C. R. S. da Silva and C. Scherer, Nucl. Instrum. Methods Phys. Res. B **18**, 1149 (1985).
[30] A. E. Volkov, Nucl. Instrum. Methods Phys. Res. B **193**, 376 (2002).
[31] C. R. A. Catlow, Proc. R. Soc. London, Ser. A **333**, 533 (1977).
[32] T. Omata, K. Okuda, S. Tsugimoto, and S. Otsuka-Matsuo-Yao, Solid State Ionics **104**, 249 (1997).
[33] H. Yokoi, Y. Arita, T. Matsui, H. Ohno, and K. Kobyashi, J. Nucl. Mater. **238**, 163 (1996).
[34] M. Bolech, E. H. P. Cordfunke, A. C. G. van Genderen, R. R. van der Lann, F. J. J. G. Janssen, and J. C. van Miltenburg, J. Phys. Chem. Solids **58**, 433 (1997).
[35] J. A. Labrincha, J. R. Frade, and F. M. B. Marques, J. Mater. Sci. **28**, 3809 (1993).
[36] R. Vassen, X. Cao, F. Tietz, D. Basu, and D. Stöver, J. Am. Ceram. Soc. **83**, 2023 (2000).
[37] M. P. Dijk, K. J. de Vries, and A. J. Burggraaf, Solid State Ionics **9&10**, 913 (1983).
[38] L. Landau and E. Lifchitz, *Théorie de l'élasticité* (MIR, Moscow, 1967).
[39] V. I. Aleksandrov, V. V. Osiko, A. M. Prokhorov, and V. M. Tatarintsev, *Current Topics in Materials Science* (North-Holland, Amsterdam, 1978), pp. 421-480.
[40] P. K. Schelling, S. R. Phillpot, and P. Keblinski, Phys. Rev. B **65**, 144306 (2002).
[41] G. Suresh, G. Seenivasan, M. V. Krishnaiah, and P. Srirama Murti, J. Nucl. Mater. **249**, 259 (1997).
[42] N. Mott and M. Littleton, Trans. Faraday Soc. **34**, 485 (1938).
[43] In our previous study Ref. 20, we used shell model with the following conditions for cations and anions: $Q^{\text{core}}+Q^{\text{shell}}=Q^{\text{formal}}$.
[44] H. Takamura and H. L. Tuller, Solid State Ionics **134**, 67 (2000).
[45] A. Banarjee, N. Adams, J. Simons, and R. Shepard, J. Phys. Chem. **89**, 52 (1985).
[46] M. Kilo, G. Borchardt, B. Lesage, O. Kaïtasov, S. Weber, and S. Scherrer, J. Eur. Ceram. Soc. **20**, 2069 (2000).
[47] H. O. Kitchner, L. P. Kubin, and V. Pontikis, *Computer Simulation in Materials Science*, Vol. 308 of NATO Advanced Studies Institute, Series E (Plenum, New York, 1995).
[48] R. D. Levine and R. B. Bernstein, *Molecular Reaction Dynamics* (Oxford University Press, New York, 1974).
[49] W. Windl, T. J. Lenosky, J. D. Kress, and A. F. Voter, Nucl. Instrum. Methods Phys. Res. B **141**, 61 (1996).
[50] R. E. Williford, R. Devanathan, and W. J. Weber, Nucl. Instrum. Methods Phys. Res. B **141**, 94 (1998).
[51] M. W. Thompson, *Defects and Radiation Damage in Metals* (Cambridge University Press, Cambridge, 1969).
[52] J. F. Ziegler, J. P. Biersack, and U. Littmark, *The Stopping Range of Ions in Solids* (Pergamon, New York, 1985).
[53] T. Karakasidis and P. J. D. Lindan, J. Phys.: Condens. Matter **6**, 2965 (1994).

[54] L. Verlet, Phys. Rev. **159**, 98 (1967).
[55] A. I. Ryazanov, V. V. Dremov, and M. Kiritani, Radiat. Eff. Defects Solids **157**, 209 (2002).
[56] C. Schäfer, H. M. Urbassek, L. V. Zhigilei, and B. J. Garrisson, Comput. Mater. Sci. **24**, 421 (2002).
[57] C. P. Flynn, *Point Defects and Diffusion* (Clarendon, Oxford, 1972).
[58] R. Volgelsang and C. Hoheisel, Phys. Chem. Liq. **16**, 189 (1987).